Acta Materialia 283 (2025) 120563

Contents lists available at ScienceDirect

Acta Materialia

journal homepage: www.elsevier.com/locate/actamat

Full length article

Creep and failure at metal-oxide interfaces

Shen J. Dillon [a,*], Ryan M. Schoell [b], Andrew Wright [c], Jian Luo [c], Eugen Rabkin [d], Khalid Hattar [e]

[a] Department of Materials Science and Engineering, University of California Irvine, 92697, Irvine, CA, United States
[b] Sandia National Laboratories, 87185, Albuquerque, NM, United States
[c] Department of NanoEngineering, University of California San Diego, 92093, La Jolla, CA, United States
[d] Department of Materials Science and Engineering, Technion – Israel Institute of Technology, 3200003, Haifa, Israel
[e] Department of Nuclear Engineering, University of Tennessee, Knoxville, 37996, TN, United States

ARTICLE INFO

Keywords:
Metal-oxide interface
Phase boundary
Creep
Deformation
Grain boundary

ABSTRACT

Small-scale bicrystal creep experiments were performed on contacts formed via *in situ* high-temperature diffusion bonding of metal-oxide interfaces including Ag-ZrO_2, Pd-ZrO_2, Pt-ZrO_2, and Ag-high entropy oxide. This work characterizes deformation and failure at metal-oxide interfaces during mechanical loading. Interfacial sliding can be activated easily, while tensile interfacial creep was not observed at any condition of stress or temperature measured. Plastic strain, instead, localizes within the metal under tensile loading. A variety of mechanisms for plastic strain occur in the metal including lattice dislocation-mediated plasticity, twinning, low-angle grain boundary formation, and low-angle grain boundary creep. Surface and low-angle grain boundary diffusion occur under conditions where no metal-oxide tensile creep is observed, highlighting the significant differences in their interfacial mechanical response. High-temperature interfacial failure occurs when the mean curvature at the contact neck is approximately zero and the applied stresses comparable to brittle fracture stresses. The brittle fracture stresses were measured to be $\sigma_f = 180 \pm 90$ *MPa* at the Ag-ZrO_2 interface at 225 °*C*, $\sigma_f = 460 \pm 160$ *MPa* at the Pd-ZrO_2 interface at 680 °*C*, and $\sigma_f = 640 \pm 440$*MPa* at the Pt-ZrO_2 interface at 1010 °*C*.

1. Introduction

Strain at metal-oxide interfaces affects the evolution and failure of a variety of technologically important materials and systems [1–13]. Stress evolution and relaxation via creep, voiding, rumpling, and spalling at metal-oxide scale interfaces strongly influences the overall oxidation resistance of refractory alloys [14,15]. Thin film stresses evolving during growth and thermal cycling must often be accommodated by the interface [16]. Complex UO_2-metal fuel cladding interactions and deformation, driven by swelling-induced stresses, can affect the lifetime of fuel rods within nuclear reactors [8]. The sintering and creep of cermets will depend strongly on sintering strain at the metal-ceramic interfaces [17,18]. Despite the importance of interfacial strain in a variety of metal-oxide systems, the process remains poorly understood.

Two general approaches for treating heterophase interfacial strain have been considered broadly. The first approach invokes a Coble creep type mechanism wherein the interface is assumed to be a perfect source and sink for point defects, and the strain rate is proportional to the interfacial diffusivity or effective viscosity [19–21]. Performing tracer diffusion measurements at phase boundaries presents a variety of practical challenges that limits the broad availability of relevant data. It also remains unclear whether the assumption that heterophase interfaces are good point defect sources and sinks is valid, as recent work suggests grain boundaries may not be good sources and sinks near equilibrium [22,23]. Irradiation based experiments have observed a range of heterophase interfacial sink efficiencies, [24] but such measurements are far from equilibrium and do not easily distinguish between Frenkel pair recombination at trapping sites in the interface and defect annihilation at sink sites at the interface. The second treatment considers the presence of [25] dislocations, common at such interfaces, as mediators of interfacial sliding [26–29]. Equilibrium misfit dislocations, which exist to minimize the interfacial energy, at flat interfaces tend to have Burgers vectors, $\vec{b}$, laying within the interfacial plane, enabling interfacial sliding in response to shear stresses, as is observed in experiments and simulations [26–30]. Interfacial sliding and/or

* Corresponding author.
E-mail address: sdillon1@uci.edu (S.J. Dillon).

https://doi.org/10.1016/j.actamat.2024.120563
Received 1 June 2024; Received in revised form 27 September 2024; Accepted 11 November 2024
Available online 13 November 2024

associated grain rotation can occur absent diffusion, via pure glide of interfacial dislocations with appropriate $\vec{b}$ [31]. Lateral rigid body motion of the interface may also occur via a diffusional flux across the entire interface. Diffusion-mediated strain normal to the interface, such as the Coble mechanism, requires point defect sources and sinks within the interfaces, typically in the form of interfacial disconnections, i.e. line defects with Burgers vectors and/or steps, with out-of-plane $\vec{b}$ components [32,33]. Fig. 1 provides a schematic depicting the qualitative differences between a pure shear mediating disconnection (Fig. 1a), a pure climb mediating interfacial disconnection (Fig. 1b), a lattice dislocation (Fig. 1c), and an interfacial step (Fig. 1d).

The motion of a disconnection through an interface can mediate a total strain, ε, of the order of the Burgers vector divided by the grain size, d. The anticipated content of pre-existing climb mediating disconnections at a given interface remains unclear for any given system. After mediating a fixed amount of strain associated with the pre-existing disconnection content and annihilating via interactions with triple junctions or other disconnections, subsequent strain requires disconnection nucleation. Indeed, recent experiments and models based on single phase bicrystal and polycrystalline creep indicate that the non-Newtonian portion of the grain boundary creep response is described well by disconnection nucleation kinetics [22], where triple junctions are considered as the primary nucleation sites. The analysis indicates that the local stresses associated with grain boundary disconnection nucleation are large, often of the order 10^8 *Pa*, and a relatively large fraction of the heterogeneous lattice dislocation nucleation stress [22]. Creep occurs experimentally at stresses much lower than these nucleation stresses [34], and the discrepancy can be rationalized by considering stress concentrations [22] that evolve at critical points like triple junctions [35,36].

High-strain bicrystal tensile creep has been demonstrated at Al_2O_3-$GdAlO_3$ interfaces, indicating that climb mediating disconnections may be accommodated by phase boundaries in systems of similar bonding character [37]. Notably, creep in that system occurred with significant off-axis deformation induced by rotation of the interfacial plane away from the loading axis. Similar bicrystal grain boundary tensile creep occurred primarily linearly along the loading axis. The off-axis deformation observed at the phase boundary, presumably, results from this interface having fewer disconnection modes available to mediate the strain homogeneously along the tensile axis. For example, the grain boundary can easily reorient via the motion of steps with small or no Burgers vector content, i.e. grain boundary migration. Immiscible phase boundaries, however, do not exhibit grain growth, restricting one mechanism for interfacial response to stress. For hard-soft interfaces like many metal-oxide systems, the difference in mechanical properties could further influence the deformation modes relative to phase boundaries in many metal-metal or oxide-oxide systems. The schematics in Fig. 1b and c highlight the hypothesis for why these interfaces may behave differently. A climb mediating disconnection could be produced by adding an interstitial loop to a metal-oxide interface. A metallic interstitial loop would require atomic relaxations around its perimeter to minimize its strain energy, analogous to what would occur around a dislocation in the bulk. Since oxides have larger shear moduli they are unlikely to relax this strain as efficiently as the metal. This is depicted schematically in Fig. 1b and c, where the atomic planes around the interstitial loop are shown to be more strained in the metal adjacent to the oxide interface than for the same loop forming as a dislocation. The interstitial loop at the interface would likely be higher in energy than the same loop in the metal lattice assuming the excess strain at the disconnection would induce more non-linear strain than the dislocation. This assumption does not have to be true generally but may be reasonable in many circumstances. In such a case, plasticity would localize in the metal rather than at the metal-oxide interface. Note that Fig. 1 is highly schematic and that the nucleation of dislocations and disconnections likely occurs heterogeneously at interfaces and other line defects rather than the homogenously, as depicted. The nature of interfacial and lattice dislocations and their nucleation is clearly more complex than the simple schematic in Fig. 1. The basic hypothesis it implies, that climb mediating interfacial dislocations may be unfavorable at some metal-oxide interfaces, motivates our question as to how metal-oxide interfaces mediate tensile strain.

The goals of the proposed work are to i) understand whether interfacial creep occurs at metal-oxide interfaces, ii) determine if climb mediating disconnection modes nucleate at metal-oxide interfaces and efficiently mediate tensile creep, and iii) define the conditions for failure are at metal-oxide interfaces at high temperatures. Metal film on oxide de-wetting experiments suggest metal diffusion at metal-oxide interfaces is active [12]. More direct chemical tracer measurements of Au at a Ni-Al_2O_3 interface produced metal-oxide interfacial diffusivity values, $D_{int} = 2.217 \times 10^{-6} exp\left(\frac{179\ kJ/mol}{RT}\right) m^2 s^{-1}$, intermediate between the metal lattice and grain boundary diffusivities in Ni [38]. Similar results have been calculated for diffusion at metal-nonmetal interfaces [39]. The occurrence of random walk diffusion does not require the existence of interfacial point defect sources and/or sinks. The absence of climb mediating disconnections, however, would extinguish any creep response even under such conditions where diffusion coefficient, D, is high, i.e. $Dt \geq x^2$, where x is a characteristic diffusion distance and t is time. Performing creep measurements at temperatures where diffusion is relatively fast could, ideally, provide insights into the thermodynamics of climb mediating disconnection nucleation at metal-oxide

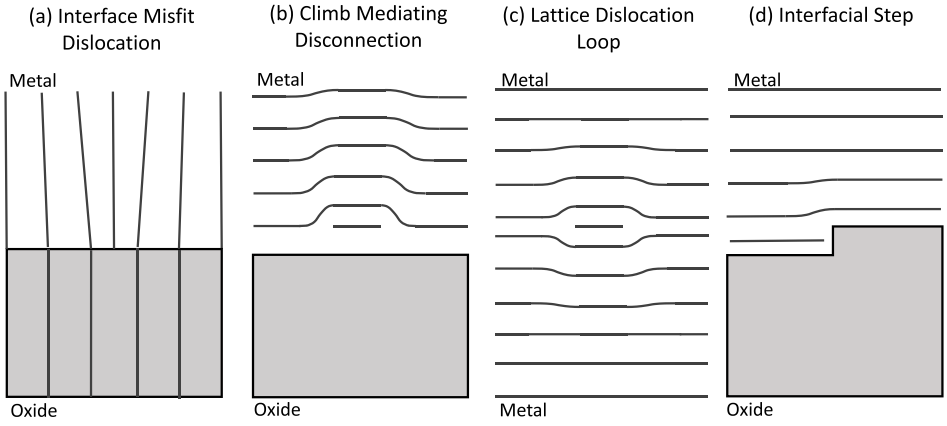

Fig. 1. Schematic of line defect structures showing (a) an interfacial misfit dislocation that mediates shear at a metal-oxide interface, (b) a climb mediating disconnection loop at a metal-oxide interface, (c) a lattice dislocation in a metal, and (d) an interfacial step. Note that the strain associated with the loop in (b) will localize primarily in the metal inducing much larger local strains than the lattice dislocation loop in (c).

interfaces.

Understanding interfacial failure during long-range diffusional transport is non-trivial. For example, a thin polycrystalline wire of fixed length and grains of constant volume will undergo a Plateau-Rayleigh instability that debonds the interface under no applied stress [40]. For grains of constant volume, a tensile stress will cause the interfaces to be less stable against debonding [41]. Tensile creep experiments involving long-range surface diffusional fluxes, where the volume is not conserved, may result in geometries that are resistant to a Plateau-Rayleigh instability, i.e. interfacial debonding. The problem might be formulated as a purely mechanistic one by considering the work of adhesion, or as a capillary problem considering the balance between sintering and de-sintering under stress. However, few experiments have probed this problem at length scales on the order of characteristic diffusion distances that would inform or validate such models.

This work is performed to provide some initial insights into the nature of interfacial deformation modes and failure at metal-oxide interfaces. Bicrystal creep experiments are performed in systems based on Ag-ZrO_2, Pd-ZrO_2, Pt-ZrO_2, and Ag-high entropy oxide (HEO) under tensile and shear loading. The investigation began as a focused effort to probe the interfacial response of Ag-oxide interfaces. Due to the propensity for plasticity to localize in the Ag lattice, the work expanded to consider noble FCC metals with higher shear moduli, Pd and Pt. These metals should also exhibit varying levels of oxide-metal interfacial adhesion resulting from their different oxygen affinities. The measurements also provide insights into how metal-oxides deform, and the importance of point defect sink structure, i.e. disconnections, in affecting interfacial creep.

2. Experimental procedure

Sc_2O_3-doped ZrO_2, subsequently referred to as ZrO_2 for simplicity, and a HEO sample, namely $[(Sm_{1/4}Eu_{1/4}Gd_{1/4}Yb_{1/4})_2(Ti_{1/2}Hf_{1/4}Zr_{1/4})_2O_7]_{0.75}$ $[(Sc_{0.266}Dy_{0.248}Tm_{0.246}Yb_{0.240})_3NbO_7]_{0.25}$ (in the barely ordered pyrochlore structure, just before the occurrence of an order-disorder transition to form the disordered defect fluorite structure at room temperature; see Wright et al. [42]) were prepared following methods described in previous work [42–45]. Samples were mechanically thinned to a thickness of several micrometers using diamond lapping films of descending particle size from 30 μm to 1 μm. 99.9 % Ag, 99.9 % Pd, and 99.9 % Pt powders were acquired from Alfa Aesar. These materials were selected for their varying bulk moduli, consistent crystal structure, and oxidation resistance. Mechanical tests were performed using a Bruker/Hysitron PI-95 picoindenter. One piece of oxide was placed on the 'sample' side of the picoindenter and another needle shaped specimen was placed on the 'indenter' side of the picoindenter. A sharp tip was formed at the end of this needle shaped sample via bicrystal tensile creep of the oxide tip contacted to the oxide substrate following experiments like those reported previously in Vikrant et al. [43]. In this process, contact between the oxide tip and oxide substrate forms a grain boundary that is deformed under conditions that induce bicrystal tensile creep. A nanowire is formed at the oxide tip apex, and its diameter is controlled by the grain boundary diffusivity. The formation mechanism for these tips can be observed in this study by observing the bicrystal creep results in the metal and subsequent capillary relaxation. The same sequence of steps was applied to the oxide samples to produce fine tips. This oxide tip was then used here to form a contact with the metal particle. Metallic powder was dispersed on the oxide prepared for the sample side of the tester by mechanically contacting the sample and the metal powder. These metal powders were pre-annealed *in situ* using laser heating to ensure that they were well-sintered. Fig. S2 shows example *in situ* sintering data to provide insights into the length scales of the particle clusters and grain sizes.

Experiments were performed using either the I^3TEM at Sandia National Laboratories, a highly modified JEOL 2100 LaB_6 source transmission electron microscope (TEM) [46] or a JEOL 2010 LaB_6. Both microscopes are equipped with a 1064 nm laser utilized for *in situ* sample heating. Both have laser spots of diameter $\approx 50\ \mu m$. The initially nanograined ZrO_2 tip on the indenter side was coarsened *in situ* using laser heating until its end was single crystalline. The metallic powder of the sample side was initially heated until it sintered to a density where no pores between particles were observable. This also ensured that the metal powder was well bonded to the substrate. The metal layer is several micrometers thick, but still significantly smaller than the diameter of the laser spot. The benefit of utilizing this sandwich structure consisting of oxide-metal powder-oxide relates to the relatively symmetric thermal impedance of the geometry. A balanced thermal impedance produces a smaller thermal gradient across the specimen and minimizes the expected thermal drift. The contacts between the indenter tip and the metal tend to be much smaller in area than between the metal and oxide substrate on the sample side. As a result, the stresses are the highest at the metal-oxide tip contact region. It is unlikely that the metal and oxide absorb similar amounts of energy and it is challenging to predict which absorbs more laser power. The temperatures, however, are not too inconsistent with those in ZrO_2 at similar laser powers measured in prior studies on ZrO_2 [43]. For example, the Pd on ZrO_2 was measured to be 218 °C at 2.4 W, while prior measurements of ZrO_2 alone yielded the temperature of 172 °C at the same power. Although, such difference is not negligible, prior experiments and COMSOL simulations suggest that for sample geometries relevant for the present study the temperature differences in excess of 100 °C are not stable over length scales of a few microns, and the corresponding temperature gradients are of the order of one °C/μm. Furthermore, the time constants for local equilibration are short relative to the timescale of the experiments, e.g. < 1 s. The respective time constants have been determined experimentally in ZrO_2 by measuring the mechanical strain in response to a change in the laser power.

Experiments were initiated by contacting the oxide tip and the metal particles and allowing them to sinter and equilibrate. Tensile loading was then induced by applying constant displacement rates. Displacement rates between 1 $nm\ s^{-1}$ and 1000 $nm\ s^{-1}$ were employed. Specific rates were selected at each temperature to probe the rates at or below which interfacial fracture occurred and above which excessive neck growth occurs at the metal-oxide interface. For some experiments, residual metal could remain adhering to the oxide tip. In these cases, the tip was moved away from the sample and laser heating was used to evaporate the metal *in situ* to avoid any possibility of metal grain boundary formation near the tip upon contact. Temperature was calibrated based on lattice parameter expansion measured from *in situ* electron diffraction assuming a linear thermal expansion coefficient in each case and utilizing room temperature as a reference value [37,43]. Fig. S3 shows an example lattice parameter expansion measurement in Ag on ZrO_2. The measurement employs a custom Matlab code that searches for peaks in the image based on initial manually input lattice vectors, calculates lattice strain, and plots it versus laser power. This approach may introduce some error in the reported temperature, but the emphasis of this work primarily relates to interfacial deformation phenomena rather than explicit kinetic rates. It is, however, possible to measure metal grain boundary and surface diffusivities from these experiments and compare with literature values to ensure they are of the correct order of magnitude. In total, tensile loading experiments were performed on metal-oxide contacts approximately 133 times for Ag-ZrO_2, 42 times for Pd-ZrO_2, 105 times for Pt-ZrO_2, and 48 times for Ag-HEO. The results discuss the general phenomena observed in these tests.

Video data was acquired at 5-15 frames per second using a Tietz videos and image processing system (TVIPS) or Gatan camera on the JEOL 2100 and 2010 TEMs, respectively, and load-displacement data was obtained at ≈100-500 points per second. These data were analyzed using custom MATLAB codes. The outlines of the samples' silhouettes were identified using an edge-finding routine based on a combination of thresholding and the edge intensity gradient. The routine utilized a

moving window algorithm to trace along each edge of the feature of interest. After identifying the edges of the bicrystal geometry the centerline of the structure is calculated. From this line, the radius, r, is calculated at each point along the length of the feature.

The average radius of the surface profile, H, is averaged from the two distances from the center line at a given position along the sample, s. To calculate the principal curvatures, $A = tan^{-1}(dH, ds)$ was calculated and used to define $\kappa_1 = cos(A)\frac{dA}{dS}$, and $\kappa_2 = -\frac{cos(A)}{H}$ assuming a conical geometry. We define the mean curvature, K, here such that neck curvature is positive when densification is favorable and negative when it is not. This is primarily for convenience of representing the data on log plots. The mean curvature at each point is defined as, $K = \kappa_1 + \kappa_2$. The load values at each point in time were calculated based on an average of approximately 10 points closest to the time in the video. These average loads were divided by πr^2 at each point along the length to approximate the applied tensile stress, σ, assuming a circular cross-section. An engineering strain was approximated using the displacement from the load-displacement curve normalized to an initial length, which is somewhat arbitrary given the approximately conical nature of some of the contacts. The initial length was, however, defined systematically in our MATLAB code based on a maximum lateral pixel deviation from the centerline of the contact. Solid-solid interfacial diffusivity, i.e. grain or phase boundary, was calculated based on the Coble creep model, which for a bicrystal takes the form: $D_i = \frac{R^2 kT}{2\pi t_c \sigma \Omega}$, where R is the radius at interface, kT is thermal energy, t_c is a time constant, defined as the ratio of the Burgers vector length to the displacement rate, σ is stress, and Ω is the atomic volume.

3. Results

3.1. Low temperature response

At sufficiently low temperatures, all systems exhibited brittle fracture at the metal-oxide interface. Fig. 2 shows example stress-strain curves for metal-oxide contacts formed *in situ*. These samples did not exhibit appreciable plastic deformation under the testing conditions. The average fracture stress, σ_f, for; the Ag-ZrO_2 interface at 225 $^{\circ}C$ was $\sigma_f = 1.8 \times 10^8 \pm 0.9 \times 10^8$ Pa, the Pd-ZrO_2 interface at 528 $^{\circ}C$ was $\sigma_f = 4.6 \times 10^8 \pm 1.6 \times 10^8$ Pa, and the Pt-ZrO_2 interface at 1010 $^{\circ}C$ was $\sigma_f = 6.4 \times 10^8 \pm 4.4 \times 10^8$ Pa. Although the comparison is not made at the same temperature, the results generally agree with the anticipated trend that metal-oxide adhesion should increase with the oxygen affinity, ϑ, of the metal; $\vartheta_{Ag} < \vartheta_{Pd} < \vartheta_{Pt}$.

3.2. Intermediate temperature response

At high homologous temperatures, all the systems exhibit a similar response, wherein plasticity localizes in the metal, as discussed in detail below. The Ag-oxide systems, however, exhibit a deformation response distinct from the other systems at intermediate temperatures, wherein lattice plasticity precedes interfacial debonding. Fig. 3 shows time-lapse images of a Ag-HEO sample strained in tension at 5 $nm\ s^{-1}$ and 275 $^{\circ}C$, along with the load-displacement response. Corresponding videos are provided as supporting data Video V1, which corresponds to Fig. 3 and Video V2 that demonstrates the tests repeatability. In each case, deformation localizes in the Ag and leads to elongation and necking of the Ag as the displacement distance increases. At the same time, the Ag-oxide interface remains almost pinned to be of a fixed width. As necking occurs away from the interface, the Ag near the interface evolves into an 'elephant foot' shaped geometry. At some critical condition, discussed more below, the interface debonds. After debonding, the asperity formed during creep rapidly smooths itself via surface self-diffusion, indicating its diffusivity is appreciable at this temperature and length scale. Despite this, no apparent interfacial creep is observed during tensile straining under these conditions. It is impossible to conclude interfacial strain is zero, since a very small amount of interfacial strain would be difficult to separate from the large amount of lattice plasticity. The resolution of the interfacial diffusion measurement is discussed in more detail below. As highlighted below, the stresses at the metal-oxide interface in this temperature range tend to be close to the interfacial failure stress. Any tensile strain at the interface would, thus, be occurring very close to its failure stress. The evolution of this structure differs dramatically from ZrO_2 bicrystals [43] and Al_2O_3-$GdAlO_3$ interfaces [37] tested in creep, where the bulk geometry remained fixed while strain localized to the grain boundaries or phase boundaries.

Although the mechanical tester employed does not perform lateral shear loading, it is possible to manipulate the indenter laterally using the piezoelectric controls. The associated stresses are not explicitly known; however, little elastic strain or bulk plasticity occurs during the interfacial shearing that accompanies lateral motion of the tip. Fig. 4 shows the same interface being deformed in shear and then subsequently loaded in tension. No apparent interfacial tensile creep was observed at the interface, despite its ability to accommodate shear. Both observations are consistent with our hypothesis that shear mediating misfit disconnections should be present, glissile in response to applied stress, and easy to nucleate.

The Ag-oxide interfaces fail at intermediate temperatures at sufficiently high stresses and/or strains. In most cases, metal-oxide interface debonding was accompanied by considerable off-axis deformation and rotation of the Ag structure just prior to or during debonding. This off-axis deformation is apparent in the time dependent plots of the sample profile, such as shown in Fig. 3b, where the last several profiles deviate dramatically in both lateral position and shape when compared to the earlier profiles; see other examples in Fig. S5. When debonding was observed via this dramatic geometric evolution, an associated grain boundary had formed within the Ag adjacent to the Ag-oxide interface. Grain boundary formation was observed via two processes. First, Ag

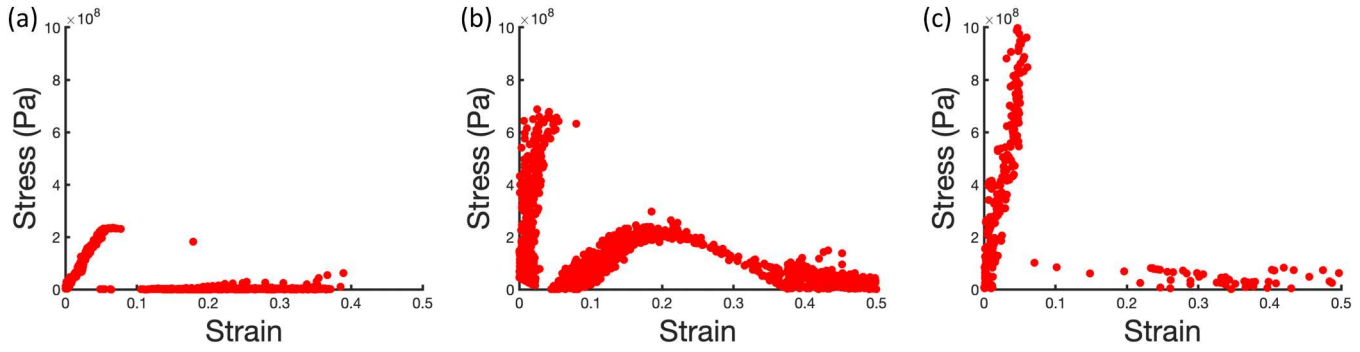

Fig. 2. Engineering stress-strain curves for (a) Ag-ZrO2, (b) Pd-ZrO2, (c) and Pt-ZrO2 at 225 $^{\circ}C$, 528 $^{\circ}C$, and 1010 $^{\circ}C$, respectively. Each interface fractures by ≈0.1 strain; the stress at intermediate strains in (b) occurs upon unloading when contact is re-established.

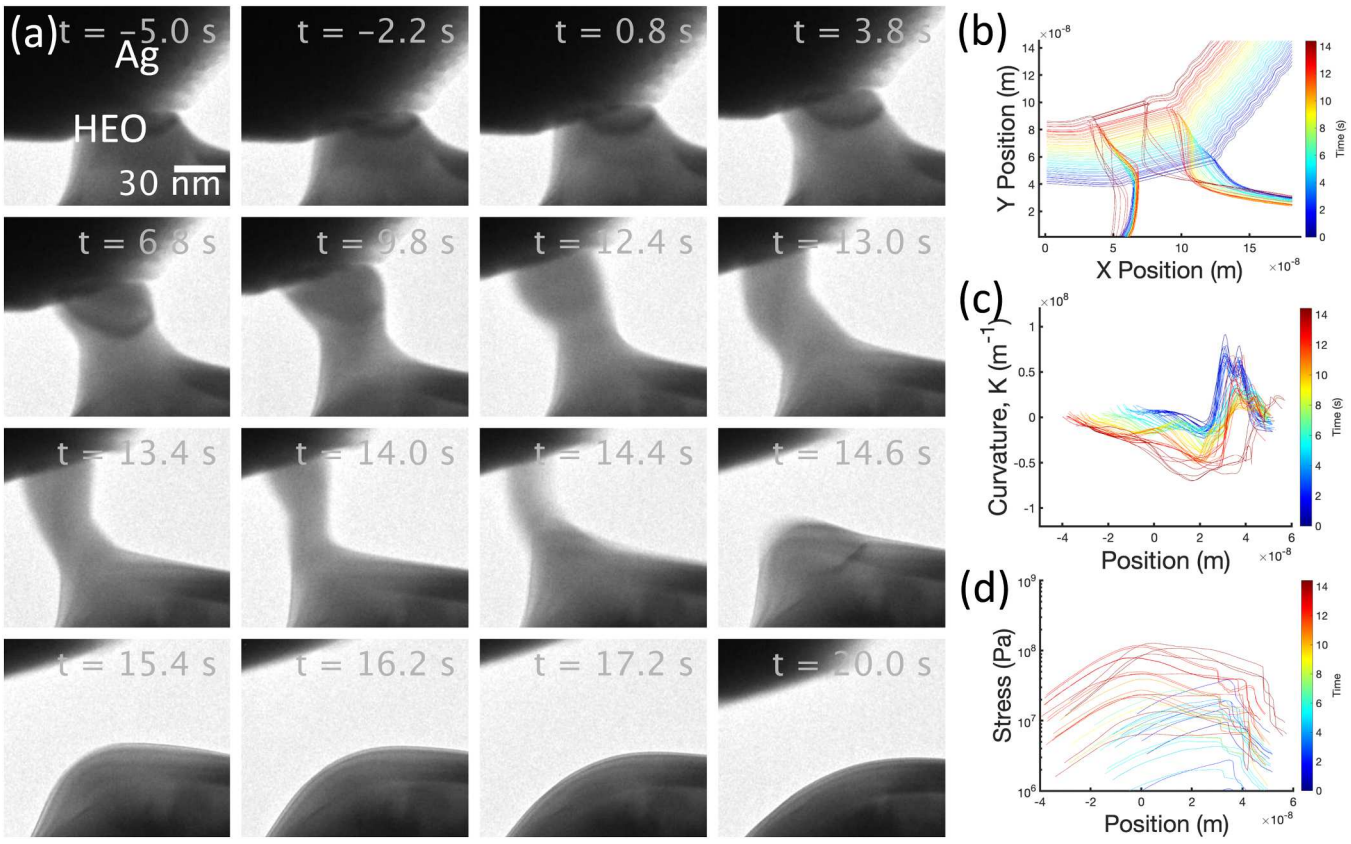

Fig. 3. (a) time-lapse images of Ag-HEO bicrystal under tensile loading along with (b) the profile of the surface developed prior to debonding, (c) the mean curvature, *K*, average for both boundaries, along the surface of the sample in each frame and (d) the calculate stress at each position along the length of the sample in each frame. Note that the onset of mechanically applied displacement occurs at t = 0 s.

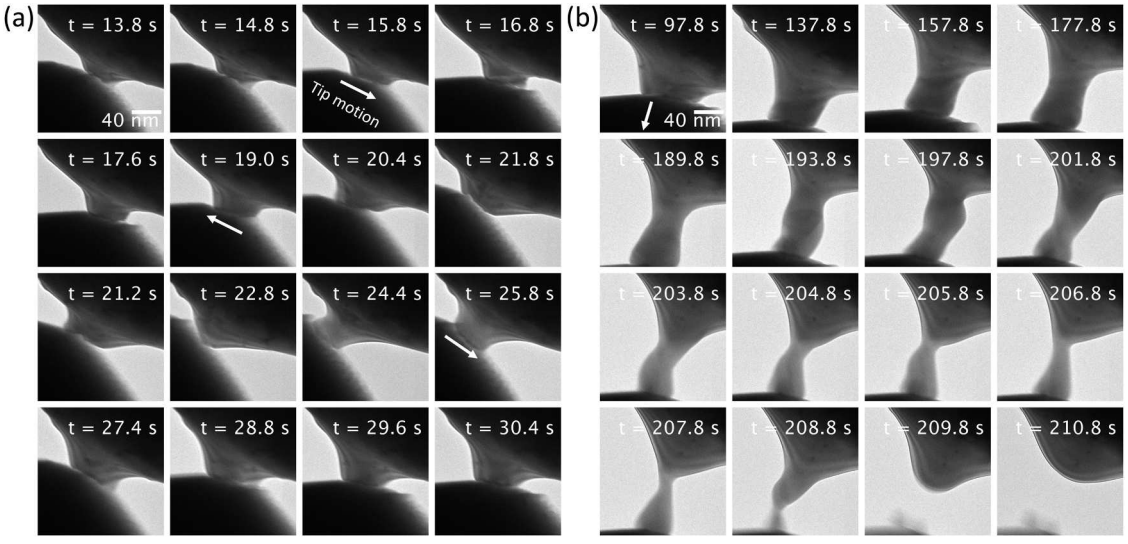

Fig. 4. (a) Time-lapse images of Ag-HEO bicrystal interface deforming in shear at 275 °*C*, where the white arrows indicate the direction of motion of the HEO 'tip'. (b) Time-lapse images of the same bicrystal interface subsequently deformed in tension at the same temperature.

twins often nucleated intersecting the Ag-oxide interface, see red arrow in Fig. 5a. Motion of the twins into positions where they became fully load bearing often preceded the off-axis deformation and rotation of the Ag. Second, low-angle grain boundaries appeared to nucleate from networks of lattice dislocations. Fig. 5b provides an example where several dislocations are observed in the lattice in one frame and in the next frame a grain boundary appears accompanied by disappearance of the dislocations. Little is known about how dislocation networks collapse into low-angle grain boundaries, but these data imply that it is a discrete process on a timescale faster than ≈0.1 *s*. The formation of these low-angle grain boundaries subsequently induces significant off-axis deformation and rotation of the adjacent grains. In several cases, at 325 °*C*, the interface debonded simply, see Fig. 5c (and supporting information), without any off-axis deformation or rotation. In these cases,

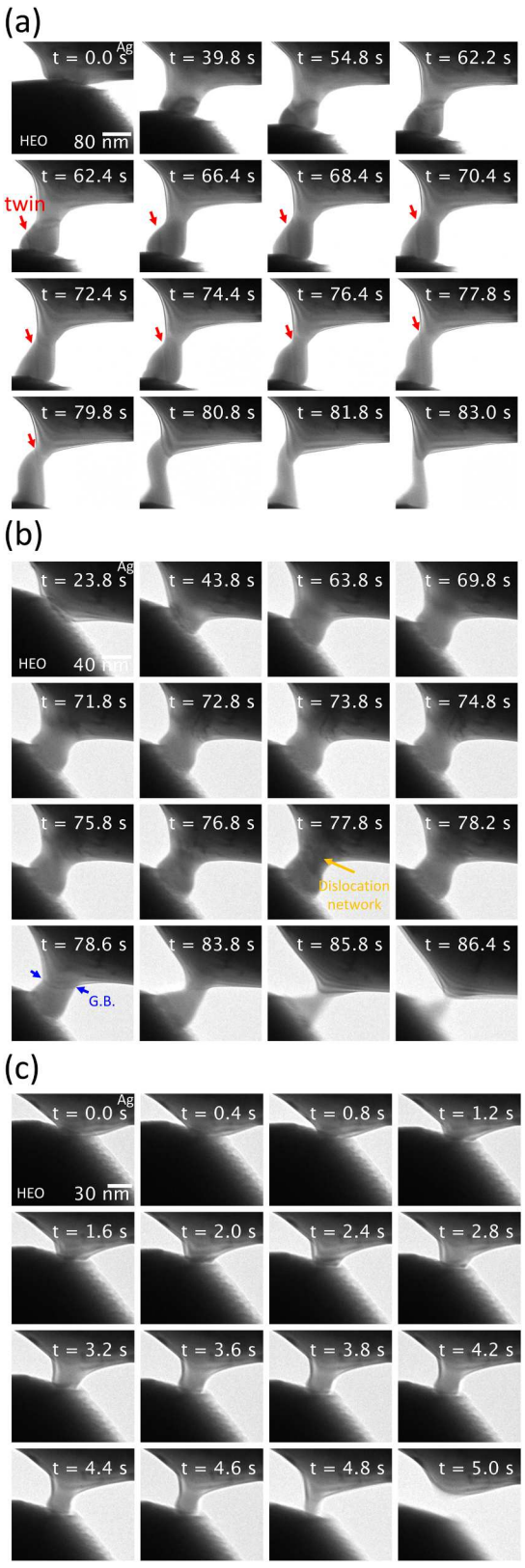

Fig. 5. Time-lapse image sequences highlighting different deformation phenomena observed in the Ag-ZrO_2 system at 275 °C. (a) twin formation and motion highlighted by the red arrow that tracks the position of the twin. (b): Dislocations collapse into a grain boundary that subsequently pinches off. (c) Pinch-off occurring at the metal-oxide interface after lattice deformation only.

no grain boundaries were observed in the Ag adjacent to the Ag-oxide interface. In several cases, debonding at the interface was also accompanied by large rotational deformation of the Ag asperity where no grain boundary was observed, see Fig. S12. In these cases, such deformation could be a response to anisotropy in surface tension, although the associated stresses may be too low to induce plastic deformation. Alternatively, the relaxation of a network of lattice dislocations could also induce such plasticity, possibly biased by surface energy anisotropy. Finally, pinch-off of Ag grain boundaries, rather than debonding of the metal-oxide interface, was also observed in several cases.

The stress and curvature profiles along the length of a sample, as shown in Fig. 3c and d, provide instructive insights into the conditions for debonding. It should be noted that these profiles describe both the metal and ceramic surfaces. The position of the interface is typically associated with the maximum peak in curvature along the profile. Due to its larger radius of curvature at the oxide portion of the interface, a stress drop is apparent at the interface entering the oxide. The maximum stress may be plotted as a function of strain to provide some insights into the average flow stress in the deforming Ag, see Fig. 6a. For comparison, the applied interfacial tensile stress may also be calculated at each instance, as plotted in Fig. 6b. The maximum stress initially occurs at the interface, but then evolves towards the plastically necked region as it becomes thinner than the interfacial contact. Just prior to failure, the interfacial width decreases, causing the maximum stress to occur at the interface once again. During the debonding phase of the evolution the load becomes quite small, and the data has larger errors. The curvature at the Ag-oxide interface may also be obtained for each frame and plotted, along with the stress, versus strain, as shown in Fig. 6b. In all cases, the curvature either remains approximately constant or decreases slightly with increasing strain. Debonding tends to occur when the curvature at the neck, in units m^{-1}, is approximately equal to the magnitude of the tensile stress, in units *Pa*. The surface energy of Ag is of the order $\gamma_{s.Ag} \approx 1\ J\ m^{-2}$ [47], accounting for the discrepancy in units. Interfacial failure should occur when the sum of the applied stress, σ_a, and the sintering stress, $\sigma_s \approx \gamma_s \kappa$, is positive, i.e. $\sigma_a + \sigma_s > 0$. Note that $\kappa < 0$ for sintering in our convention. The load on the thin Ag structure towards the end of the experiment is sufficiently low, so that its value may be affected by the noise level of the measurement. Nevertheless, $\sigma_a \approx \sigma_s$ appears to be of the correct magnitude at failure. The magnitude of σ_a at the Ag-oxide interface at failure is also in general agreement with the interfacial brittle fracture strength of $\sigma_f \approx 1.8 \times 10^8\ Pa$.

An alternative formulation of the debonding response is as follows. $\sigma_a = \sigma_s$ is the so-called zero-creep condition where neither densification nor creep will occur. For a wire geometry of fixed length, *L*, the Plateau-Rayleigh instability criterion predicts interface debonding or de-sintering when $\frac{L}{r} > 2\pi$ [48]. Interfaces are always less stable against Plateau-Rayleigh instabilities than single crystals [49]. For a simple wire geometry the zero-creep stress is expressed as $\sigma_z = \frac{\gamma_s}{r}\left(1 - \frac{\frac{\gamma_g}{\gamma_s}}{\frac{L}{r}}\right)$, where *r* is the wire radius and γ_g is the grain boundary energy. For $L \gg r$, at the zero-creep condition $\sigma_z r = \sigma_s r = \gamma_s \kappa_1 r \approx 1$. Our geometry is not ideally cylindrical, but an alternative formulation of a similar concept follows that $K = 0$ when $\kappa_2 = \kappa_1$. $\kappa_2 \sim \frac{1}{R}$ so $\kappa_1 R \approx 1$ should represent the point where the system transitions from sintering to de-sintering. Fig. 6c plots $\kappa_1 R$ versus strain. Similar example data may be found in the supporting data. This average value at just prior to debonding is $\kappa_1 R = 1.67 \pm 0.73$. This value may be a bit larger than an ideal value due to the propensity to underestimate κ_1 when it becomes very large just prior to failure, i.e. on the order of several pixels. This, nevertheless, agrees well with the anticipated debonding condition given the simplifying geometric assumptions. The value of this interfacial curvature-based failure criterion, albeit approximate, is that it does not rely on measurements of applied stress at debonding where the loads are small and does not

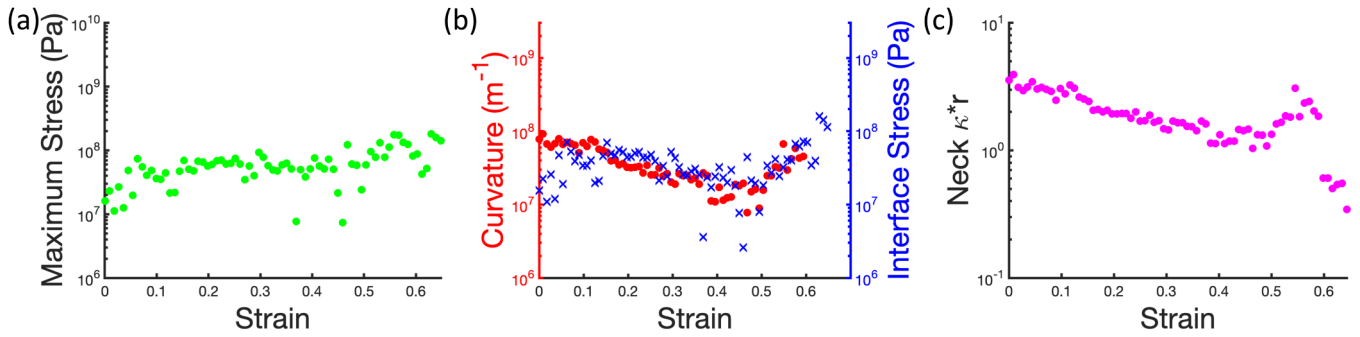

Fig. 6. Data calculated from the results shown in Fig. 3, including; (a) the maximum stress as a function of strain, b) the mean curvature, K, and stress at the metal-oxide interface versus strain, and c) the product of the interfacial radius and neck radius of curvature, $\kappa_1 R$, versus strain.

require a fixed volume assumption for the grains.

3.3. High temperature response

Above 375 $^{\circ}C$ in the Ag-ZrO_2 system and above 567 $^{\circ}C$ in the Pd-ZrO_2 system, all tensile experiments produced no apparent deformation at the metal-oxide interface, bulk plasticity over some range of strain, followed by the formation of a low-angle grain boundary. This grain boundary subsequently facilitated bicrystal Coble creep and/or bulk plasticity as shown in Fig. 7a-b. Videos V3 and V4 show examples of this process. The Pt-ZrO_2 system behaved differently because its grain size remained smaller after pre-sintering. Deformation of the pre-existing grain boundaries was observed in some cases, see Fig. 7c, rather than plasticity-induced GB formation. The geometric areas of these Pt grain boundaries tended to be larger than the area of the Pt-ZrO_2 interface suggesting that the phase boundary yield strength far exceeded the grain boundary yield strength. Due to the lower lattice and/or grain boundary yield strengths exhibited by the metals at higher temperatures, the metal-oxide interfaces never reached the fracture stress, or the debonding condition $\sigma_a \approx \sigma_s$. Similar example data may be found in the supporting information.

Grain boundary bicrystal creep in Ag at 375 $^{\circ}C$ occurs at a stress comparable to bulk plasticity as indicated by the two processes occurring in parallel in regions of similar width. Multiple grain boundaries formed during tensile loading in many cases, indicating that bulk plasticity continued to nucleate new grain boundaries even as other grain boundaries were creeping. At 430 $^{\circ}C$ and higher temperatures, only grain boundary creep is observed, and often only one boundary is observed during tensile loading. Such a transition from lattice creep to mixed mode lattice and grain boundary creep, to pure grain boundary creep, with increasing temperature is generally anticipated due to differences in apparent activation energies for the two processes [50]. During steady-state low angle grain boundary tensile creep, the condition $\kappa_1 R \approx 1$ at the grain boundary, see supplementary Figs. S13-S16 and S20, is often observed. This suggests that the boundary is close to the interfacial failure condition in the Coble regime. This is consistent with the hypothesis that disconnection nucleation requires large stresses, comparable to lattice dislocation nucleation. It is also consistent with observations that creep cavitation is not avoidable for stresses at, or even below, those associated with the Coble regime [51].

Bicrystal creep of Ag can also induce twin formation, presumably due to the low stacking fault energy of the system; see Fig. S23. Tensile creep mediating disconnections are inherently non-equilibrium defects. The observation of twin formation suggests that the grain boundary may access a variety of non-equilibrium disconnection modes as the creep process dissipates energy. Twinning has also been observed to accommodate grain boundary migration [52] and plasticity [53]. Similar twins were not observed in Pd or Pt, presumably due to their higher stacking fault energies. It is interesting that deformation twinning in bulk coarse grain Ag has been observed only at the temperatures lower than room temperature [54].

3.4. Surface diffusion and grain boundary diffusion

The surface diffusivity after interfacial failure and low angle grain boundary diffusion after their formation may be approximated to pro-

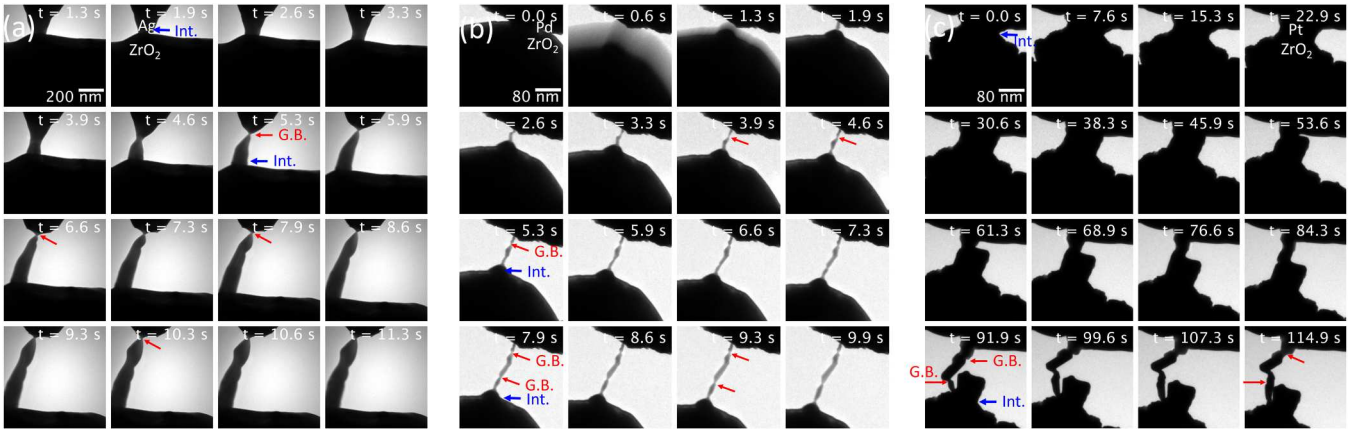

Fig. 7. Time-lapse image sequences of (a) Ag-ZrO_2, (b) Pd-ZrO_2, and (c) Pt-ZrO_2 grain boundary creep at 380 $^{\circ}C$, 567 $^{\circ}C$, and 1435 $^{\circ}C$respectively. In (a) the newly formed grain boundary (GB) may be observed at 5.3 s. A slight rotation of the relative orientation of the grain below the boundary relative to the loading axis is also apparent upon the formation of the neck. In (b) the GB forms after an initial fracture at 0.6s which reforms a new contact with a low angle grain boundary after 1.3. In (c) the Pt initial contacting the ZrO_2 (Int.) adheres and deformation occurs within th Pt ultimately forming an eloganted grain with grain boundaries that undergoes grain boundary creep.

vide a reference for diffusional transport kinetics. Nichols and Mullins [55] described the rate of capillary smoothing of conical tips when rate limited by surface diffusion. The radius of curvature, r_t, of conical tips is described by:

$$r_t^4 - r_{t,o}^4 = A_\alpha \frac{D_s \gamma_s \Omega^2 \nu}{kT}(t - t_o)$$

and the motion of the tip position, z_t, is similarly described by:

$$z_t^4 - z_{t,o}^4 = B_\alpha \frac{D_s \gamma_s \Omega^2 \nu}{kT}(t - t_o)$$

where A_α and B_α are independent geometric factors that depend on the cone half-angle and are shown if Fig. S24, ν is the concentration of surface diffusion mediating defects taken as $\nu = \Omega^{-2/3}$, D_s is the surface diffusivity, t is time, and γ_s is the surface energy, assumed to be $\gamma_s \approx 1$ J m^{-2}. Note, z_t is defined by the path along which the peak of the tip moves, in the ideal conical geometry defined by the model it would be the central axis of the cone. Fig. 8 plots the tip position versus time for Ag, tested against ZrO_2, at $T \approx 350\,^\circ C$ and $T \approx 410\,^\circ C$. The response ideally follows quartic scaling, but this assumes that the angle of the conical geometry behind the tip is constant, which is not followed explicitly in all cases. Both data follow this scaling reasonably well for the example shown at $T \approx 350\,^\circ C$. However, the data at $T \approx 410\,^\circ C$ only follow the appropriate trend in the early or late stage of the experiment for the radius of curvature and tip position, respectively. This results from the significant change in the geometry of the tip, assumed in the model to be conical, as it evolves. Regardless, it is possible to approximate reasonable surface diffusivity values. Similar examples are also shown in the Figs. S25-S28. An overall fit to the data produces a somewhat large apparent activation energy, $D_s = 1.7 \times 10^{17} exp\left(\frac{301\ kJ/mol}{RT}\right) m^2 s^{-1}$, which could result from a variety of factors such as a change in diffusion mechanism or surface structure with temperature that could also be influenced by temperature dependent surface segregation. There is a large scatter of data on Ag surface self-diffusion in the literature depending on measurement method and annealing ambient. Temperature dependent changes in activation energy have been observed in Ag that would produce large apparent activation energies [56]. The values for surface diffusivity obtained here are close to those obtained by Winegard and Chalmers using radiotracer method and annealing in nitrogen [44]. At higher temperatures, the interface did not fail during tensile loading, so analogous measurements were not possible.

Fig. S29 provides low angle grain boundary diffusivity measurement distributions obtained from Ag. Figs. S30-S34 show examples of low angle Pd grain boundary creep experiments data. The low angle grain boundary diffusivities measured in Ag are $D_{Ag,GB} = 6.3 \times 10^3 exp\left(\frac{117\ kJ/mol}{RT}\right) m^2 s^{-1}$, which is slightly lower than expected for high angle grain boundaries in FCC metals, while the Pd values, $D_{Pd,GB} = 1.7 \times 10^3 exp\left(\frac{276\ kJ/mol}{RT}\right) m^2 s^{-1}$, align closely with the literature values. These results support our hypothesis that these measurements are not strongly influenced by the presence of the electron beam in these experiments.

4. Discussion

Fig. 9 provides a schematic highlighting the deformation response observed in this study. No apparent or appreciable tensile creep is observed at the metal-oxide interfaces studied here even at stresses greater than the lattice yield strength and the low-angle grain boundary yield strength measured directly in the same experiments. Shear of the metal-oxide interface, however, can be activated at stresses below the lattice yield strength. Metal-oxide interfacial deformation modes requiring little or no diffusion are, therefore, active while diffusion dependent modes are not under conditions tested. Under tension plasticity localizes in the metal via a combination of dislocation mediated creep, and grain boundary formation and grain boundary mediated creep. At Ag-oxide interfaces deboning occurred at higher strains and lower temperatures, but was not observed at high temperatures or the other metal systems.

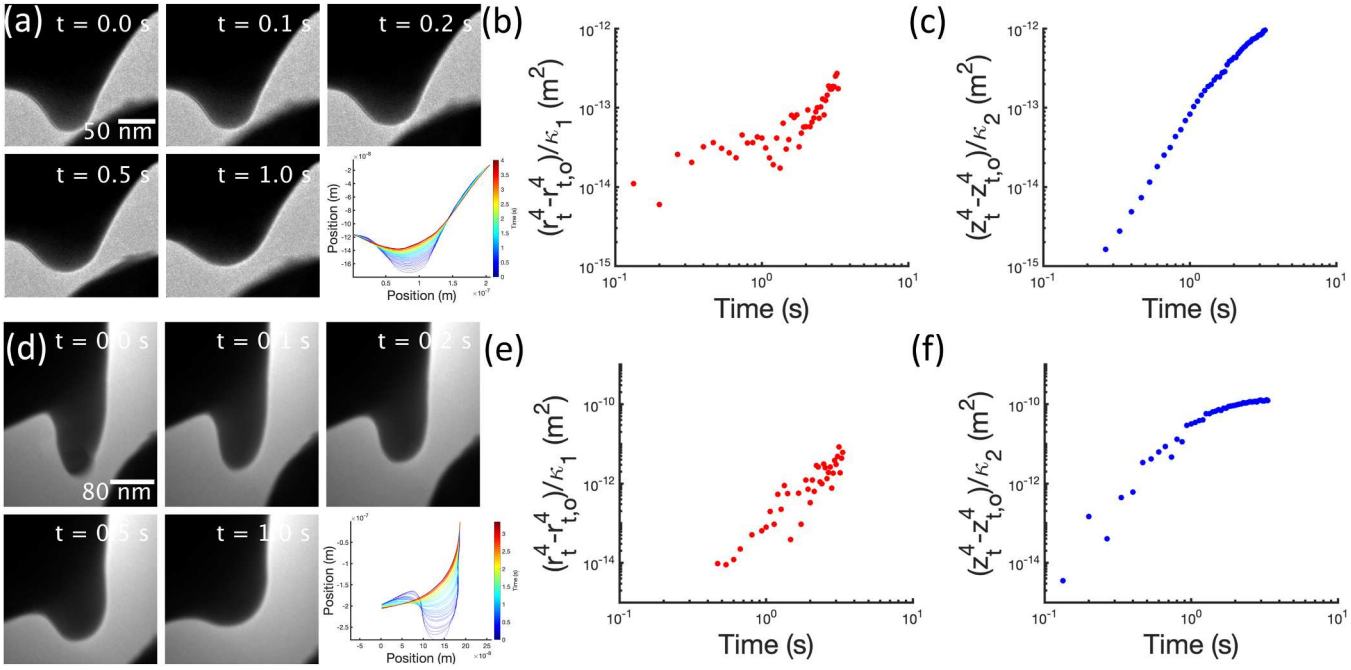

Fig. 8. (a) time-lapse image sequence of Ag capillary smoothing after interfacial debonding along with inset showing the surface profile in each frame, (b) the associated tip radius of curvature, and (c) the tip position along the direction of its motion at $T \approx 350\,^\circ C$. (d-f) provides the same type of data but at $T \approx 410\,^\circ C$. $\kappa_1 = A_\alpha \frac{D_s \gamma_s \Omega^2 \nu}{kT}$ and $\kappa_2 = B_\alpha \frac{D_s \gamma_s \Omega^2 \nu}{kT}$ where the cone half-angle defining A_α and B_α are calculated at each time.

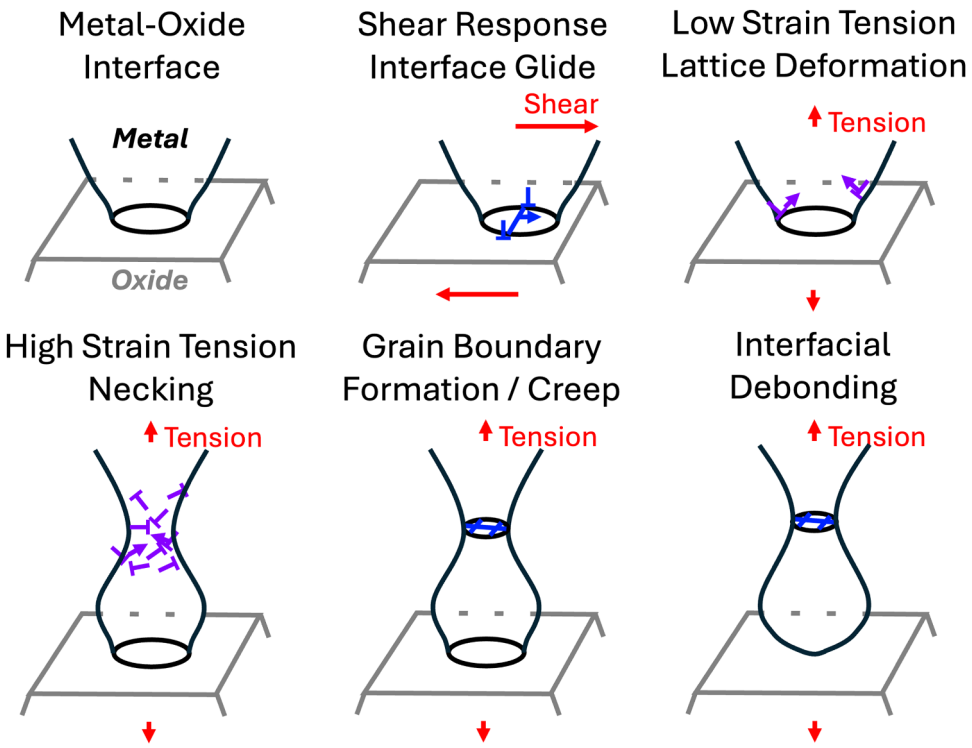

Fig. 9. Schematic depicting the primary deformation mechanisms active in this study.

Two possible interpretations could be invoked for rationalizing the lack of tensile creep at the metal-oxide interfaces during these experiments. First, nucleation of climb mediating disconnections is unfavorable at the metal-oxide interface, inhibiting tensile creep regardless of the interfacial diffusivity. Second, interfacial diffusion is too sluggish to resolve any interfacial creep. The only direct measurement of metal-oxide diffusion that the authors are aware of used Au as a chemical tracer at a Ni-Al_2O_3 interface [38]. Fig. 10 plots this data along with average values for face-centered cubic metal grain boundary and lattice diffusivity, [57,58] and calculated values for Al at an Al-Si interface [39] on an Arrhenius plot normalized to melting temperature, T_m. The plot also contains Ag surface diffusion, Ag low angle grain boundary diffusivity, and Pd low angle grain boundary diffusivity measured in this study. The experimental resolution of our creep experiments is also plotted together with this data. The comparison suggests that our experiments produce a measurement resolution comparable to the tracer measurement. However, extrapolation of the tracer measurements to higher temperatures suggests the measurement should be able to resolve this level of diffusion under some testing conditions employed in this study. It should also be noted that Au tracer diffusion in Ni is slower than Ni self-diffusion[59], and Au transport along a Ni-Al_2O_3 interface may be exothermic due to the stronger Ni-O bond strength relative to Au-O. Both arguments suggest that the tracer measurement might underestimate interface diffusion slightly relative to self-diffusion. If relevant, however, these chemical effects should not change the order of magnitude. The comparison is, indeed, challenging, since the null result, i.e. no interfacial strain, could be interpreted as either diffusion or nucleation rate limited without direct isotopic tracer measurements performed on the identical interface. This comparison can support the hypothesis that sluggish diffusion may account for the low creep rates. Alternatively, the fact that metal-oxide interfacial yield strength far exceeds the metal grain boundary yield strength and the lattice yield strength, can support the hypothesis that nucleating climb mediating disconnections at the metal-oxide interface is unfavorable. Indeed, both arguments may be valid; interfacial diffusion is sluggish and climb mediating disconnection nucleation is unfavorable. For example, it may not be a coincidence that the first paper arguing for the need to invoke interface reaction controlled kinetics to describe interfacial creep used data from the Au-Al_2O_3 system to motivate the problem [60].

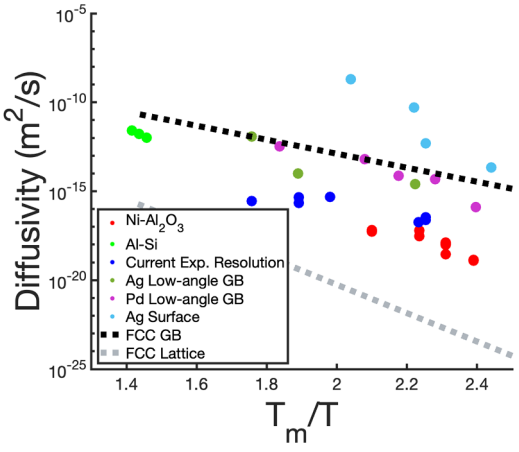

Fig. 10. Arrhenius plot normalized to homologous temperature of the metal showing approximate values for grain boundary and lattice diffusivity in FCC materials [57,58], Au tracer diffusivity at a Ni-Al_2O_3 interface [38], Al diffusivity at an Al-Si interface calculated by molecular dynamics [39], Ag low angle GB diffusion from this work, Ag surface diffusion from this work, and the experimental resolution of experiments performed on Ag-oxide interfaces in the current work.

Generally, it can be concluded that grain boundary creep exceeds metal-oxide interfacial creep by at least several orders of magnitude at the same temperature. Furthermore, metal-oxide interfacial deformation is highly anisotropic, with interfacial sliding [61] occurring much more readily than tensile deformation. This should affect the stress relaxation processes and deformation modes at these interfaces. For example, surface rumpling [14] and diffusion mediated interfacial debonding [62] often occurs at thin oxide scales on metal alloys formed via oxidation. The rumpling of the metal could indicate the favorability

of interfacial sliding [63] accommodated by metal plasticity as a mechanism for stress relaxation. Void formation is consistent with the limited ability of these interfaces to deform in tension.

In addition to observations of metal-oxide interfacial deformation modes, the work also reveals several interesting phenomena discussed briefly below. For example, plasticity-induced low-angle grain boundary formation during bicrystal tensile straining was observed. Understanding the mechanisms for the process are outside of the scope of the current work and quantitative theoretical models describing them are largely absent from the existing literature. These measurements provide some initial insights into the amounts of local stresses, strains, and dislocation densities associated with the period just prior to grain boundary formation.

In Ag, lattice deformation and grain boundary creep occurred in parallel under many testing conditions. This suggests that lattice dislocation depinning from obstacles or their generation by the dislocation sources is occurring at stresses of similar magnitude as grain boundary disconnection nucleation, in this case on the order of $10^7 - 10^8$ *Pa*, and at similar local strain rates. A model for grain boundary creep was recently developed based on the assumption that stress concentrations at singular points, such as triple junctions, facilitate disconnection nucleation at lower applied stresses [22]. The model suggests that the nucleation stresses for creep mediating disconnections should be comparable to those associated with nucleating lattice dislocations. The common occurrence of grain boundary creep cavitation implies that these stresses are also comparable in magnitude to the failure stress [36]. The similar magnitudes of the GB creep stress, lattice flow stress, and interfacial failure stress observed in the current study supports this general picture. As observed in this work, these different processes should exhibit different temperature dependencies causing different mechanisms to dominate in different regimes of temperature and stress, as anticipated from classical deformation mechanism maps [50].

Twin nucleation was observed in the silver lattice during low-temperature deformation (see Fig. 5a) and at the grain boundaries during bicrystal creep (see Fig. 22). The latter phenomena suggests that nucleating disconnections to mediate creep can sample those that produce twins in low stacking fault energy materials. This highlights the variety of disconnection modes accessible to a grain boundary, where their selection depends on Arrhenius kinetics [64]. The nucleation of different disconnection modes could represent statistical variations between modes with nearly degenerate activation energies. It could also result from variations in local stresses that bias nucleation towards one disconnection mode or another. Each disconnection mode should exhibit distinct activation volume tensors leading to a rich variety of deformation responses. Such concepts currently require more theoretical development. In addition to creep, other dissipative processes such as sintering, grain growth, or particle irradiation may enable grain boundaries to sample disconnection modes that do not represent the lowest energy modes under stress-free conditions. In general, a morphological similarity of the creep-generated twin observed in the present study and annealing twins observed in face-centered cubic metals with low stacking fault energy indicates the similarity of underlying atomistic mechanisms associated with disconnection nucleation. This issue could be of interest in understanding how grain boundaries generally access metastable states or overcome activation barriers associated with grain boundary phase transitions [65,66].

These experiments also provide insights into quantitative metrics for diffusion-dependent interfacial failure. Interfacial debonding at high temperatures occurs at stresses of the same magnitude as the brittle fracture stress. The behavior also generally agrees with a failure criterion based on measurements of interfacial curvature. Models for these processes, however, tend to assume constant volume grains as a boundary condition [48,49], especially when considering the influence of applied stress. Grain boundary motion or long-range surface diffusion can drive changes in grain size. This dissipative process can produce qualitatively different results than predictions based on assumptions of constant volume [49].

5. Conclusions

Tensile creep at metal-oxide interfaces was not observable at interfaces in Ag-HEO, Ag-ZrO_2, Pd-ZrO_2 and Pt-ZrO_2 at an experimental resolution of approximately $D_{resolution} = 1.41 \times 10^{11} exp\left(\frac{47\ J/mol}{R}\frac{T_m}{T}\right) m^2 s^{-1}$. The result is consistent with expectations that disconnection nucleation may be unfavorable at metal-oxide interfaces and that metal diffusion at metal-oxide interfaces is several orders of magnitude slower than grain boundary diffusion. Interfacial shear occurred much more readily at these same interfaces indicating a highly anisotropic deformation response. Under tensile loading, plasticity localizes in the metal and can induce low-angle grain boundary nucleation at sufficiently large strains, and these grain boundaries can then exhibit creep at rates consistent with grain boundary tracer diffusion reported in the literature. The results imply that metal-oxide interfacial creep is more than 2 orders of magnitude slower than grain boundary creep in the metal and slower than lattice power law creep in the metal at temperatures measured. A capillary-based analysis and a mechanical analysis were found to approximately describe high-temperature interfacial debonding, under conditions where surface diffusion was rapid, when the geometry approached $\kappa_1 R \approx 1$ or the stress at the interface approached the brittle facture stress.

CRediT authorship contribution statement

Shen J. Dillon: Writing – original draft, Methodology, Investigation, Formal analysis, Conceptualization. **Ryan M. Schoell:** Writing – review & editing, Investigation. **Andrew Wright:** Investigation. **Jian Luo:** Writing – review & editing, Resources. **Eugen Rabkin:** Writing – review & editing, Conceptualization. **Khalid Hattar:** Writing – review & editing, Resources, Methodology.

Declaration of competing interest

The authors declare that they have no known competing financial interests or personal relationships that could have appeared to influence the work reported in this paper.

Acknowledgements

Support from the US DOE Office of Basic Energy Sciences, Materials Science and Engineering Division under Grant DE-SC0023447 is gratefully acknowledged by SJD. This work was performed, in part, at the Center for Integrated Nanotechnologies, an Office of Science User Facility operated for the U.S. Department of Energy (DOE) Office of Science. Sandia National Laboratories is a multimission laboratory managed and operated by National Technology & Engineering Solutions of Sandia, LLC, a wholly owned subsidiary of Honeywell International, Inc., for the U.S. DOE's National Nuclear Security Administration under contract DE-NA-0003525. The views expressed in the article do not necessarily represent the views of the U.S. DOE or the United States Government. The UCSD subteam also acknowledges partial support from the National Science Foundation (under grant DMR-2026193) for the fabrication of compositionally complex fluorite-based oxides (the HEO) used in this study.

Supplementary materials

Supplementary material associated with this article can be found, in the online version, at doi:10.1016/j.actamat.2024.120563.

References

[1] J. Robertson, M.I. Manning, Limits to adherence of oxide scales, Mater. Sci. Technol. 6 (1) (1990) 81–92.
[2] A.G. Evans, M.Y. He, J.W. Hutchinson, Mechanics-based scaling laws for the durability of thermal barrier coatings, Prog. Mater. Sci. 46 (3) (2001) 249–271.
[3] H. Assadi, F. Gartner, T. Stoltenhoff, H. Kreye, Bonding mechanism in cold gas spraying, Acta Mater. 51 (15) (2003) 4379–4394.
[4] R. Dauskardt, M. Lane, Q. Ma, N. Krishna, Adhesion and debonding of multi-layer thin film structures, Eng. Fract. Mech. 61 (1) (1998) 141–162.
[5] G.M. Pharr, W.C. Oliver, Measurement of thin-film mechanical-properties using nanoindentation, MRS Bull. 17 (7) (1992) 28–33.
[6] A.A. Volinsky, N.R. Moody, W.W. Gerberich, Interfacial toughness measurements for thin films on substrates, Acta Mater. 50 (3) (2002) 441–466.
[7] P. Hofmann, D. Kerwinpeck, UO2/ZIRCALOY-4 chemical interactions from 1000-degrees-C TO 1700-degrees-c under isothermal and transient temperature conditions, J. Nucl. Mater. 124 (1984) 80–105.
[8] N. Marchal, C. Campos, C. Garnier, Finite element simulation of Pellet-Cladding Interaction (PCI) in nuclear fuel rods, Comput. Mater. Sci. 45 (3) (2009) 821–826.
[9] L. Yuan, Y. Wang, R. Mema, G. Zhou, Driving force and growth mechanism for spontaneous oxide nanowire formation during the thermal oxidation of metals, Acta Mater. 59 (6) (2011) 2491–2500.
[10] H. Barda, L. Klinger, E. Rabkin, Microstructure evolution of thin nickel films with embedded chromium oxide nanoparticles, Acta Mater. 201 (2020) 561–571.
[11] L. Klinger, E. Rabkin, On the nucleation of pores during the nanoscale Kirkendall effect, Mater. Lett. 161 (2015) 508–510.
[12] A. Kumar, H. Barda, L. Klinger, M.W. Finnis, V. Lordi, E. Rabkin, D.J. Srolovitz, Anomalous diffusion along metal/ceramic interfaces, 5251, Nat. Commun. 9 (2018).
[13] S.W. Hieke, A. Frank, M.J. Duarte, H. Gopalan, P. Patil, M. Wetegrove, M. Rohloff, A. Kruth, C. Pistidda, M. Dornheim, K. Taube, G. Dehm, C. Scheu, Stability and failure mechanisms of Al2O3|Al bilayer coatings exposed to 300 bar hydrogen at 673 K, Adv. Eng. Mater. 26 (4) (2024) 2300619.
[14] V.K. Tolpygo, D.R. Clarke, Surface rumpling of a (Ni, Pt)Al bond coat induced by cyclic oxidation, Acta Mater. 48 (13) (2000) 3283–3293.
[15] F. Gaudette, S. Suresh, A.G. Evans, G. Dehm, M. Rühle, The influence of chromium addition on the toughness of γ-Niα-Al2O3 interfaces, Acta Mater. 45 (9) (1997) 3503–3513.
[16] F. Spaepen, Interfaces and stresses in thin films, Acta Mater. 48 (1) (2000) 31–42.
[17] J. Zackrisson, H.O. Andrén, U. Rolander, Development of cermet microstructures during sintering, Metallurg. Mater. Trans. A 32 (1) (2001) 85–94.
[18] S.T. Mileiko, Oxide-fibre/Ni-based matrix composites—III: a creep model and analysis of experimental data, Compos. Sci. Technol. 62 (2) (2002) 195–204.
[19] F. Ernst, METAL-oxide interfaces, Mater. Sci. Eng. R-Rep. 14 (3) (1995) 97–156.
[20] J. Rosler, M. Baker, M. Volgmann, Stress state and failure mechanisms of thermal barrier coatings: role of creep in thermally grown oxide, Acta Mater. 49 (18) (2001) 3659–3670.
[21] M. Gasik, B.S. Zhang, A constitutive model and FE simulation for the sintering process of powder compacts, Comput. Mater. Sci. 18 (1) (2000) 93–101.
[22] S.J. Dillon, E. Lang, S.C. Finkeldei, J.-h. Ouyang, K. Hattar, A nucleation rate limited model for grain boundary creep, Acta Mater. 246 (2023) 118718.
[23] S.J. Dillon, S.C. Finkeldei, E. Lang, K. Hattar, A.T. Nelson, Using in situ UO2 bicrystal sintering to understand grain boundary dislocation nucleation kinetics and creep, J. Am. Ceramic Soc. 107 (10) (2024) 6701–6714.
[24] S. Mao, S. Shu, J. Zhou, R.S. Averback, S.J. Dillon, Quantitative comparison of sink efficiency of Cu–Nb, Cu–V and Cu–Ni interfaces for point defects, Acta Mater. 82 (2015) 328–335.
[25] Z. Zhang, Y. Long, S. Cazottes, R. Daniel, C. Mitterer, G. Dehm, The peculiarity of the metal-ceramic interface, Sci. Rep. 5 (1) (2015) 11460.
[26] E.G. Fu, N. Li, A. Misra, R.G. Hoagland, H. Wang, X. Zhang, Mechanical properties of sputtered Cu/V and Al/Nb multilayer films, Mater. Sci. Eng. A-Struct. Mater. Propert. Microstruct. Process. 493 (1-2) (2008) 283–287.
[27] R.G. Hoagland, R.J. Kurtz, C.H. Henager, Slip resistance of interfaces and the strength of metallic multilayer composites, Scr. Mater. 50 (6) (2004) 775–779.
[28] A. Misra, M. Verdier, Y.C. Lu, H. Kung, T.E. Mitchell, N. Nastasi, J.D. Embury, Structure and mechanical properties of Cu-X (X=Nb,Cr,Ni) nanolayered composites, Scr. Mater. 39 (4-5) (1998) 555–560.
[29] J. Wang, A. Misra, An overview of interface-dominated deformation mechanisms in metallic multilayers, Curr. Opin. Solid State Mater. Sci. 15 (1) (2011) 20–28.
[30] L. Wang, Y. Zhang, Z. Zeng, H. Zhou, J. He, P. Liu, M. Chen, J. Han, D.J. Srolovitz, J. Teng, Y. Guo, G. Yang, D. Kong, E. Ma, Y. Hu, B. Yin, X. Huang, Z. Zhang, T. Zhu, X. Han, Tracking the sliding of grain boundaries at the atomic scale, Science (1979) 375 (6586) (2022) 1261–1265.
[31] C. Qiu, M. Salvalaglio, D.J. Srolovitz, J. Han, Disconnection flow–mediated grain rotation, Proc. Natl. Acad. Sci. 121 (1) (2024) e2310302121.
[32] E. Arzt, M.F. Ashby, R.A. Verrall, Interface controlled diffusional creep, Acta Metallurgica 31 (12) (1983) 1977–1989.
[33] M.F. Ashby, Interface-reaction control of Nabarro-Herring creep and sintering, Scr. Met. 3 (11) (1969) 837–842.
[34] B. Burton, Interface reaction controlled diffusional creep: A consideration of grain boundary dislocation climb sources, Mater. Sci. Eng. 10 (1972) 9–14.
[35] R. Raj, M.F. Ashby, Intergranular fracture at elevated temperature, Acta Metallurgica 23 (6) (1975) 653–666.
[36] H. Trinkaus, M.H. Yoo, Cavity nucleation under time-dependent stress concentrations, Philos. Mag. A 57 (4) (1988) 543–564.
[37] D.K. Coffman, Y. Ma, C.M. Barr, J.-h. Ouyang, K. Hattar, S.J. Dillon, Interphase boundary, grain boundary, and surface diffusion in Al2O3/GdAlO3 composites determined from bicrystal coble creep experiments, J. Eur. Ceram. Soc. 42 (9) (2022) 3976–3985.
[38] H. Barda, E. Rabkin, Metal hetero-diffusion along the metal-ceramic interfaces: A case study of Au diffusion along the Ni-sapphire interface, Acta Mater. 186 (2020) 242–249.
[39] I. Chesser, R.K. Koju, A. Vellore, Y. Mishin, Atomistic modeling of metal–nonmetal interphase boundary diffusion, Acta Mater. 257 (2023) 119172.
[40] O. Hussein, D. Keith Coffman, K. Hattar, E. Lang, S.J. Dillon, F. Abdeljawad, Plateau–rayleigh instability with a grain boundary twist, Appl. Phys. Lett. 121 (14) (2022).
[41] L. Klinger, E. Rabkin, Thermal stability and creep of polycrystalline nanowires, Acta Mater. 54 (2) (2006) 305–311.
[42] A.J. Wright, Q. Wang, C. Hu, Y.-T. Yeh, R. Chen, J. Luo, Single-phase duodenary high-entropy fluorite/pyrochlore oxides with an order-disorder transition, Acta Mater. 211 (2021) 116858.
[43] K.S.N. Vikrant, R.L. Grosso, L. Feng, E.N.S. Muccillo, D.N.F. Muche, G. S. Jawaharram, C.M. Barr, A.M. Monterrosa, R.H.R. Castro, R.E. Garcia, K. Hattar, S.J. Dillon, Ultrahigh temperature in situ transmission electron microscopy based bicrystal coble creep in zirconia I: Nanowire growth and interfacial diffusivity, Acta Mater. 199 (2020) 530–541.
[44] D. Zhang, Y. Chen, H. Vega, T. Feng, D. Yu, M. Everett, J. Neuefeind, K. An, R. Chen, J. Luo, Long- and short-range orders in 10-component compositionally complex ceramics, Adv. Powder Mater. 2 (2) (2023) 100098.
[45] D. Zhang, Y. Chen, T. Feng, D. Yu, K. An, R. Chen, J. Luo, Discovery of a reversible redox-induced order-disorder transition in a 10-component compositionally complex ceramic, Scr. Mater. 215 (2022) 114699.
[46] K. Hattar, D.C. Bufford, D.L. Buller, Concurrent in situ ion irradiation transmission electron microscope, Nucl. Instrument. Method. Phys. Res. Sect. B: Beam Interact. Mater. Atom. 338 (2014) 56–65.
[47] E.R. Funk, H. Udin, J. Wulff, Surface Tension of Solid Silver, JOM 3 (12) (1951) 1206–1208.
[48] F.F. Lange, De-sintering, a phenonmena concurrent with densifictation within powder compacts: a review, in: R.M. German, G.L. Messing, R.G. Cornwall (Eds.), Sintering Technology, Marcel Dekker, New York, 1996.
[49] O. Hussein, D. Keith Coffman, K. Hattar, E. Lang, S.J. Dillon, F. Abdeljawad, Plateau–Rayleigh instability with a grain boundary twist, Appl. Phys. Lett. 121 (14) (2022) 141601.
[50] M.F. Ashby, A first report on deformation-mechanism maps, Acta Metallurgica 20 (7) (1972) 887–897.
[51] J.R. Porter, W. Blumenthal, A.G. Evans, Overview 14 Creep fracture in ceramic polycrystals—I. creep cavitation effects in polycrystalline alumina, Acta Metallurgica 29 (12) (1981) 1899–1906.
[52] B. Lin, Y. Jin, C.M. Hefferan, S.F. Li, J. Lind, R.M. Suter, M. Bernacki, N. Bozzolo, A. D. Rollett, G.S. Rohrer, Observation of annealing twin nucleation at triple lines in nickel during grain growth, Acta Mater. 99 (2015) 63–68.
[53] H.G.F. Wilsdorf, The ductile fracture of metals: a microstructural viewpoint, Mater. Sci. Eng. 59 (1) (1983) 1–39.
[54] H. Suzuki, C.S. Barrett, Deformation twinning in silver-gold alloys, Acta Metallurgica 6 (3) (1958) 156–165.
[55] F.A. Nichols, W.W. Mullins, Morphological changes of a surface of revolution due to capillarity-induced surface diffusion, J. Appl. Phys. 36 (6) (1965) 1826–1835.
[56] G.E. Rhead, Surface self-diffusion of silver in various atmospheres, Acta Metallurgica 13 (3) (1965) 223–226.
[57] A.M. Brown, M.F. Ashby, Correlations for diffusion constants, Acta Metallurgica 28 (8) (1980) 1085–1101.
[58] W. Gust, S. Mayer, A. Bögel, B. Predel, Generalized representation of grain boundary self-diffusion data, J. Phys. Colloques 46 (C4) (1985) C4–537. -C4-544.
[59] M.J.H. van Dal, M.C.L.P. Pleumeekers, A.A. Kodentsov, F.J.J. van Loo, Diffusion studies and re-examination of the Kirkendall effect in the Au–Ni system, J. Alloys. Compd. 309 (1) (2000) 132–140.
[60] M.F. Ashby, On interface-reaction control of Nabarro-Herring creep and sintering, Scripta Metallurgica 3 (11) (1969) 837–842.
[61] J.W. Cahn, Y. Mishin, A. Suzuki, Coupling grain boundary motion to shear deformation, Acta Mater. 54 (19) (2006) 4953–4975.
[62] M.R. Turner, A.G. Evans, An experimental study of the mechanisms of crack extension along an oxide/metal interface, Acta Mater. 44 (3) (1996) 863–871.
[63] Z.T. Trautt, Y. Mishin, Capillary-driven grain boundary motion and grain rotation in a tricrystal: a molecular dynamics study, Acta Mater. 65 (2014) 19–31.
[64] J. Han, S.L. Thomas, D.J. Srolovitz, Grain-boundary kinetics: a unified approach, Prog. Mater. Sci. 98 (2018) 386–476.
[65] T. Frolov, D.L. Medlin, M. Asta, Dislocation content of grain boundary phase junctions and its relation to grain boundary excess properties, Phys. Rev. B 103 (18) (2021) 184108.
[66] S.J. Dillon, M.P. Harmer, G.S. Rohrer, The relative energies of normally and abnormally growing grain boundaries in alumina displaying different complexions, J. Am. Ceramic Soc. 93 (6) (2010) 1796–1802.